Journal of Chromatography A 1730 (2024) 465089

Contents lists available at ScienceDirect

Journal of Chromatography A

journal homepage: www.elsevier.com/locate/chroma

All-atom modeling of methacrylate-based multi-modal chromatography resins for Langmuir constant prediction of peptides

Tim Ballweg [a], Modan Liu [a], Julian Grimm [a], Elaheh Sedghamiz [b,c], Wolfgang Wenzel [b], Matthias Franzreb [a,*]

[a] Institute of Functional Interfaces, Karlsruhe Institute of Technology, Hermann-von-Helmholtz-Platz 1, Eggenstein-Leopoldshafen 76344, Germany
[b] Institute of Nanotechnology, Karlsruhe Institute of Technology, Hermann-von-Helmholtz-Platz 1, Eggenstein-Leopoldshafen 76344, Germany
[c] Schrödinger, GmbH, Glücksteinallee 25, Mannheim 68163, Germany

ARTICLE INFO

Keywords:
Multi-modal chromatography
Methacrylate-based polymer backbone
Molecular modeling
Langmuir constant prediction
Peptide adsorption

ABSTRACT

In downstream processing, the intricate nature of the interactions between biomolecules and adsorbent materials presents a significant challenge in the prediction of their binding and elution behaviors. This complexity is further heightened in multi-modal chromatography (MMC), which employs two distinct binding mechanisms. To gain a deeper understanding of the involved interactions, simulating the adsorption of biomolecules on resin surfaces is a focal point of ongoing research. However, previous studies often simplified the adsorbent surface, modeling it as a flat or slightly curved plane without including a realistic backbone structure. Here, we introduce and validate two novel workflows aimed at predicting peptide binding behaviors in MMC, specifically targeting methacrylate-based resins. Our first achievement was the development of an all-atom model of a commercial MMC resin surface, incorporating its polymethacrylic backbone. Furthermore, we established and tested a workflow for rapid calculations of binding free energies (ΔG) with 10 linear peptides as target molecules. These ΔG calculations were effectively used to predict Langmuir constants, achieving a high coefficient of determination (R^2) of 0.96. In subsequent benchmarking tests, our model outperformed established, simpler resin surface models in terms of predictive capabilities.

1. Introduction

Liquid preparative chromatography is an indispensable tool in the biopharmaceutical industry for the purification and separation of complex mixtures [1–3]. The process relies on the differential interactions of compounds with a stationary phase and a mobile phase [4]. A notable advancement in stationary phases was the introduction of multi-modal chromatography (MMC), where resins facilitate a combination of distinct interaction types, such as electrostatic and hydrophobic interactions, between the ligands and the molecules being separated [5–7]. This approach is particularly effective for molecules that are challenging to separate using conventional chromatographic methods [8]. Despite the advantages of MMC, it further increases the already intricate nature of the adsorption mechanism [9]. Therefore, finding ideal binding and elution conditions, especially for biomolecules, remains a complex task during the initial process development [10]. This complexity is compounded by the limited availability and high cost of product samples in the early stages of drug development, which restricts extensive empirical screening [11].

To overcome these challenges, the last few decades have seen significant efforts in developing computational modeling methods. These methods aim to predict the interactions of biomolecules with chromatographic media under various conditions. Their origins date back to the mid-20th century with the development of basic empirical models that laid the foundation for understanding the kinetics and thermodynamics of chromatographic processes [12–14]. These models evolved into more sophisticated approaches, such as mechanistic modeling, which provided a deeper understanding of chromatographic processes based on physical and chemical principles [15,16]. Since then research focused on the development of novel isotherms, like the SMA isotherm for ion exchange chromatography [17]. Also, considerable effort was made to describe the adsorption behavior for MMC by considering electrostatic or both, electrostatic and hydrophobic interaction in the isotherm equations [9,18,19].

Quantitative Structure-Property Relationships (QSPR) and Quantitative Structure-Activity Relationships (QSAR) are further modeling

* Corresponding author.
E-mail address: matthias.franzreb@kit.edu (M. Franzreb).

https://doi.org/10.1016/j.chroma.2024.465089
Received 13 March 2024; Received in revised form 11 June 2024; Accepted 12 June 2024
Available online 13 June 2024

approaches that originated in the late 1970s and early 1980s [20]. Initially based on simple correlations between molecular descriptors and chromatographic outcomes, these models have evolved to incorporate a wider range of descriptors and complex statistical methods, including machine learning [21,22]. Recent applications in multimodal chromatography have been particularly impactful, enabling the prediction of complex molecule behaviors, such as those of proteins, under various chromatographic conditions [23].

The early 2000s marked the introduction of molecular simulations in chromatography [24–28]. Advances in computational power and algorithms enabled more sophisticated and accurate simulations, providing detailed insights into molecular-level interactions within chromatographic systems [27]. These simulations have shown promising predictive capabilities for the binding and elution behavior of peptides and proteins in ion exchange [10,24,27] and multimodal chromatography [26,28].

However, most utilized molecular modeling methods are still limited by the extensive computational effort required, rendering them impractical for high-throughput screenings. Another major challenge is the accurate modeling of the chromatography resins' surface [25]. The complexity of resins, particularly their three-dimensional all-atom surface structure, is often simplified in models, by tethering the ligands to a planar surface. However, it is important to consider that, in reality, resins neither possess a planar surface nor a perfectly uniform ligand density, attributed to the nanoscale structure of the backbone. Moreover, for polymer-based chromatography resins, like methacrylate-based resins, the backbone itself can exhibit hydrophobic characteristics, which can influence the overall molecular affinity towards target molecules [29].

Addressing these challenges, we showcase in this work two molecular modeling workflows for the prediction of Langmuir constants. First, we demonstrate a workflow that creates all-atom structures of methacrylate-based chromatography resin surfaces, incorporating the polymeric backbone structure. A subsequently presented workflow facilitates rapid screenings for binding poses and energies between bespoke resin surface models and target molecules. In a final step, we benchmark the capability for Langmuir constant predictions of our all-atom model with established, more simplified models of the resin surface.

2. Material and methods

2.1. Selection of chromatography resin and target molecules

In this study, the multimodal chromatography resin TOYOPEARL MX-Trp-650M, procured from Tosoh Bioscience, was selected for use in both the computational and experimental workflows. This resin is characterized by a hydroxylated polymethacrylic backbone and is functionalized with a tryptophan (Trp) ligand through its N-terminal amino group [30]. The combination of electrostatic and hydrophobic properties of the negatively charged carboxyl group and the indole ring, respectively, enables this ligand to form complex interactions with various target molecules.

Linear peptides, acquired from Biomol GmbH were utilized as target molecules. Selection criteria included molecular weight, structural characteristics, and the net charge at pH 4, which aligns with the optimal pH for binding to the tryptophan ligand [30]. Especially the molecular size was a critical factor since it influences both the inherent flexibility of the peptides and consequently the computational simulation duration. The experimental detection of these peptides was conducted through UV absorption spectroscopy by selecting wavelengths that exhibited a maximal differential absorption relative to pure buffer solution. Table S1 (SI) enumerates all 10 peptides in addition to providing the specific wavelengths used for UV absorption measurements, molecular weights, and structural details.

2.2. All-atom resolution model of methacrylate-based resin surfaces

To construct an all-atom resolution model of the methacrylate-based resin, we developed a multiscale modeling approach which incorporates coarse-grained and atomistic molecular dynamics simulation protocols to build the polymer network structure of the resin. This model can then be leveraged in a subsequent workflow employing quantum mechanics (QM)-based methods to analyze the adsorption behavior of target molecules on the resin.

Fig. 1 provides a schematic comparison of the scale of our all-atom resin surface model relative to a chromatography column. As shown, the resin is depicted in our model as a cuboid section extracted from the inside of a particle pore. The y,x plane at the upper end in the z direction represents the interface between the stationary and mobile phase. The remaining surfaces, which are essentially the cut sides of the resin particle, might include molecule fragments.

To simulate the dynamic polymerization process, we established a simulation box containing all necessary components: a methacrylate-based monomer and crosslinker forming the polymer backbone, the ligand attached to the backbone, and a porogen to control the polymer density. To model a representative system of widely used components, the monomer chosen was 2,3-Dihydroxypropyl methacrylate (DHPMA), derived from the hydrophilization of Glycidylmethacrylate (GMA), and Ethylene glycol dimethylacrylate (EDGMA) was selected as the crosslinker. The ratio of monomer to crosslinker was set at 1:5, aligning with common practices in the field [29].

For the model's dimensions, we opted for a larger size of 10/15/15 nm (height/width/depth) than required for the adsorption simulations of peptides, to accurately capture the nanoscale structure of the surface. Due to this extended length scale, constructing an entire polymer network at an atomistic level was infeasible, especially when starting from the individual components of the selected 4-component system. To address this, we developed a multistage simulation protocol. The first step involved creating a coarse-grained (CG) representation to establish the reference topology and initial coordinates of the polymer network. This CG model was then converted into an atomistic representation, where structural relaxation yielded the final coordinates.

In the first step, a CG model was generated using a reaction rate-based model [31], that replicates the dynamic process of polymerization. In this model, employing Kremer-Grest type parametrization, DHPMA dimers were considered as single beads and EDGMA was represented by two beads. The Trp ligand, represented by a single bead, was integrated into the polymer network following the polymerization reactions. The porogen was represented solely by its size. Each bead in the CG scheme corresponded to approximately 100 Da in molecular weight and was within a $1 \times 1 \times 1$ nm length scale. For an accurate simulation of the interface between the mobile and stationary phase, the initial simulation box's upper half in the z-direction was populated with porogen beads, designed not to diffuse into the lower half. The bottom half of the box was filled with a defined mixture of monomer, crosslinker, ligand, and additional porogen. Here, generic reaction rates were applied to radical-based activation, polymerization, crosslinking, and quenching reactions, as listed in Table S2 in the SI.

The conversion in the second step involved replacing CG beads with individual DHPMA, EGDMA, and Trp molecules, optimized using LigParGen [32]. The molecules were arranged to fit within a $1.1 \times 1.1 \times 1.1$ nm box to prevent overlapping atoms post-conversion. Intermolecular bonds, such as C-C and C-N, were incorporated after decapping hydrogen atoms from bond-formation sites, and charges were reset on either side of the new bond. During the relaxation phase, the expanded simulation box was isotropically compressed to recover its original dimensions. An all-atom relaxation, following the OPLS-aa [33] parametrization, was performed with incremental timesteps, initially resolving clashes with sub-femtosecond temporal resolutions and later using a 2 fs deltaT for faster collective movement of the polymer. This polymer network generation protocol was automated within the workflow engine

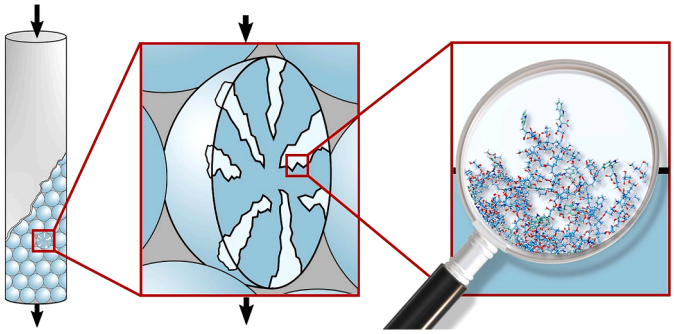

Fig. 1. Scale of All-Atom Model Compared to Chromatography Column - This illustration provides a schematic comparison between the scale of all-atom models of resin surfaces in relation to the size of a chromatography column.

of Simstack [34], and both CG and all-atom molecular dynamics simulations were executed using LAMMPS [35]. For a comprehensive view of the subsequent simulation steps, the entire workflow is presented as 'Workflow 1' in the flowchart Fig. S1 of the SI. The automated workflow is available upon request from the authors.

The structure generated from our workflow was imported into Maestro 13.7 (Schrödinger Release 2023-2) for further manual refinement. In this postprocessing stage, we removed smaller polymer molecules that were not integrated into the main polymer network and deprotonated the carboxyl groups. Subsequently, the structure was subjected to a second round of minimization using MacroModel. During this minimization, we immobilized the outermost residues on the cut edges of the particle to preserve the structural integrity. The refined structure obtained through this process served as the input for our workflows focused on determining the binding poses and energies of target molecules.

To ensure mechanical stability, which requires a dense backbone structure in reality, we carefully adjusted the quantities of DHPMA and EDGMA molecules in our initial simulation box, maintaining a constant ratio. This adjustment was done empirically by gradually increasing the number of molecules until the model exhibited a dense, crosslinked polymeric network. Following this, we increased the Trp ligand concentration to match the ideal ligand spacings of 5 to 15 Å, as commonly reported in literature for simpler models [27,28]. For the final configuration of our model, the lower half in the z-direction of the initial binding box with dimensions of 10/15/15 nm (height/width/depth) was filled with a specific molecular composition: 690 DHPMA dimers, 260 EDGMA crosslinkers, 690 Trp ligands, and 320 porogens.

2.3. Modeling of binding poses and energies

This section delineates the second pivotal workflow in our study, focusing on advanced computational methods to determine binding poses and energies between target molecules and our custom-developed all-atom models of methacrylate-based chromatography resin surfaces. Our approach utilizes computationally efficient methods, enabling fast screenings suitable for standard office computers. The entire multistep simulation was automated in KNIME Version 4.7.1 using the Schrödinger extensions from Release 2023-2. Essential inputs for this workflow are specific simulation parameters, a file containing all target molecule SMILES strings, and a docking grid of the resin model. The parameters for each simulation step are listed in Tables S2 and S3, with default settings applied where specific parameters are not mentioned. The docking grid was created using Maestro 13.6 (Schrödinger, Release 2023-2) and positioned at the center of the adsorbent model's surface with a midpoint box diameter of 40 Å in all directions.

The workflow commences with the LigPrep node, utilized for calculating the 3D structures of the target molecules from their input SMILES strings and determining their protonation states. Following this, an initial binding pose screening was performed using the Glide docking node, which generated 100 potential binding poses [36]. Next, the target-molecule-adsorbent complex with the highest docking score was subjected to a structural minimization in the MacroModel node, utilizing implicit solvent modeling and the OPLS4 force field [37]. This step was crucial for simulating the polymer backbone's flexibility during the adsorption process, an aspect not considered in the docking approach that treats the resin as rigid. For computational efficiency, atoms in the resin model located beyond 5 Å from the docking grid were fixed in place during this minimization stage.

Subsequently, the pose was refined through MM-GBSA simulations [36]. To address the issue of potential false positive binding poses, we employed the semiempirical quantum mechanics method GFN2-xTB for single-point energy calculations afterward [38]. GFN2-xTB was chosen for its balance between computational efficiency and accuracy in modeling noncovalent interactions such as π- or van der Waals interactions [39], which are significant in our system [40]. To expedite potential energy calculations, resin atoms more than 15 Å from the target molecule were removed, and the truncated model was hydrogen-saturated at the cut sites. The binding free energy (ΔG) was then calculated using the free energies of the target molecule (G_{tm}), the resin model (G_{ads}), and the complex of both (G_{com}), defined as [41–43]:

$$\Delta G = G_{com} - G_{ads} - G_{tm} \quad (1)$$

If the resulting ΔG from the GFN2-xTB calculation was more than 30 % lower than the binding energy calculated by MM-GBSA, the pose was considered a false positive. This artificial stopping criterion served as a balance between achieving precise full minimization and managing the computational cost within the high-throughput workflow. In practice, by employing single-point energy calculations, we refined ΔG and effectively identified false positive poses that may arose from earlier force-field-based minimizations.

Following the identification of a false positive pose, it was removed from consideration, and the binding pose with the next highest docking score was chosen for subsequent processing. This included another round of MacroModel minimization, followed by MM-GBSA and GFN2-xTB calculations. Once a suitable binding pose was determined, we eliminated any remaining docking poses that overlapped in volume with this pose. We then repeated the whole process three additional times. This methodical approach ensured that we obtained four distinct binding poses for each target molecule, without any overlapping volume. To illustrate the sequence of simulation steps, the complete workflow is detailed as 'Workflow 2' in the flowchart shown in Fig. S1 of the SI. The automated workflow is available upon request from the authors.

2.4. Batch incubation chromatography experiments

To validate our simulative findings, we conducted batch incubation chromatography experiments to determine the adsorption isotherms of all 10 peptides. These high-throughput experiments were carried out in

96-deepwell filter plates (Pall) using a fully automated robotic laboratory system. This automation enhanced the reproducibility and precision of our experiments while reducing manual labor.

Initially, a precise volume of chromatography resin was loaded into the filter plates using a ResiQuot (MediaScout), guaranteeing a representative distribution of particle sizes. [44]. Each well received a 7.7 μL resin plaque. The adsorption isotherms were established from 10 concentration points, derived by serially diluting a 5 g/L peptide solution in 0.1 M acetate buffer at pH 4 across 10 even steps, with a final volume of 300 μL per well. The plates were then agitated for 1 h at 1000 rpm using a shaker module (Heater Shaker Module, Opentrons).

Post-incubation, the unbound peptide solution was removed using a 96-well vacuum manifold (Perkin Elmer) connected to a vacuum pump (MD 4 VARIO select, Vacuubrand), and the filtrate was collected in a 96-deep well plate. Subsequently, 200 μL of this solution was transferred to a 96-well flat-bottom UV plate (Brand) for UV absorption measurements using a plate reader (Spark, Tecan). The specific UV wavelength for each peptide, as listed in Table S1, was used for detection. All pipetting tasks were automated using an OT-2 liquid handling station (Opentrons). The plate transfers between the devices were handled by a robotic arm (UR-5e, Universal Robot), and the entire laboratory setup was controlled via a central Python script interfacing with the application programming interfaces (APIs) of the lab components.

2.5. Comparison with state-of-the-art models

To evaluate the effectiveness of our approach, we conducted a comparative analysis between our all-atom resin surface model (AAM) and established, more simplified model approaches. Upon reviewing existing literature, we identified that the models used to represent resin surfaces generally fall into two distinct categories. The first category features models where ligands are fixed in space, creating a planar surface with uniform ligand orientation, resulting in highly symmetrical models [10,24,27,45–48]. In contrast, the second category involves ligands attached to carbon chains or similar spacer molecules, which are then connected to either a planar or curved carbon surface [28,49–51]. This configuration allows for greater ligand mobility, leading to a more disordered surface appearance after energy minimization. Most studies suggest an optimal ligand spacing ranging from 5 to 15 Å [27,28], a parameter we also targeted in our all-atom model to replicate realistic ligand densities.

We developed a model for each category using the building tool in Maestro 13.6 (Schrödinger Release 2023-2). Visual representations of the two generated models are provided in Fig. 2. In the first simplified model (SM1, shown in Fig. 2a), the ligands are uniformly oriented, each anchored in space by a single carbon atom. For the second simplified model (SM2, depicted in Fig. 2b), the ligands are attached to C12 carbon chains, which are then connected to a flat carbon surface. Before proceeding to binding free energy calculations, all models were subjected to an energy minimization using the MacroModel module. During this process, the anchoring carbon atoms in SM1 and the carbon surface, connected to the C12 chains in SM2, were fixed in place to maintain structural stability.

Following the minimization process, a docking grid featuring a midpoint box of 40 Å was centered within each model. To prevent target molecules from adsorbing to the carbon chains or areas beneath the model surface, these regions were designated as excluded volumes during grid generation. These grids then served as inputs for the workflow outlined in Section 2.3, facilitating the calculation of binding free energies with target molecules.

3. Results and discussion

3.1. All-atom resolution model of methacrylate-based resin surfaces

We successfully created an all-atom model for the TOYOPEARL MX-Trp-650M MMC resin surface, utilizing the workflow described in Section 2.2 and illustrated as 'Workflow 1' in Fig. S1 of the SI. The resulting polymeric resin's structure is depicted in Fig. 3, where the carbon atoms of the methacrylic backbone are colored blue, and the Trp ligand's carbon atoms are green. The simulation effectively generated the interface between the stationary and mobile phase, visible at the top end in the z-direction in Fig. 3a and b. This interface highlights a highly non-uniform surface, characterized by polymeric chains that extend into the mobile phase and mesopores that penetrate the entire model, as seen from the top view in Fig. 3c. Our model resulted in an average ligand spacing of approximately 12 Å, fitting within the 5 to 15 Å range reported as optimal in the literature for simpler models. However, in contrast to the more planar surfaces of established models, our model exhibits significant variation in ligand positions along the z-direction.

A notable innovation in our model is the inclusion of a methacrylic polymer backbone structure, a feature that, to our knowledge, has been implemented for the first time in the context of modeling chromatography resin surfaces. This addition provides a more complex and realistic portrayal of resin surfaces, capturing their inherent irregularities in contrast to the traditionally flatter and more uniform surfaces depicted in existing models. The detailed representation of the polymer backbone within our all-atom model not only improves the visual and structural fidelity but could also deepen our understanding of how biomolecules interact with the resin surface on a molecular level. This advancement could significantly influence the development of next-generation chromatography resins, enabling the design of materials with tailored surface properties and superior performance characteristics.

3.2. Modeling of binding poses and binding energies

To demonstrate a use case for our developed model, we successfully calculated the binding poses and energies for all peptides using the workflow outlined in Section 2.3 and illustrated as 'Workflow 2' in Fig. S1 of the SI. We identified four distinct binding poses for each peptide within the docking grid. Notably, during the minimization step, significant conformational changes in the polymer were observed in response to peptide adsorption.

Fig. 4 presents a binding pose of Octapeptide-2 interacting with the

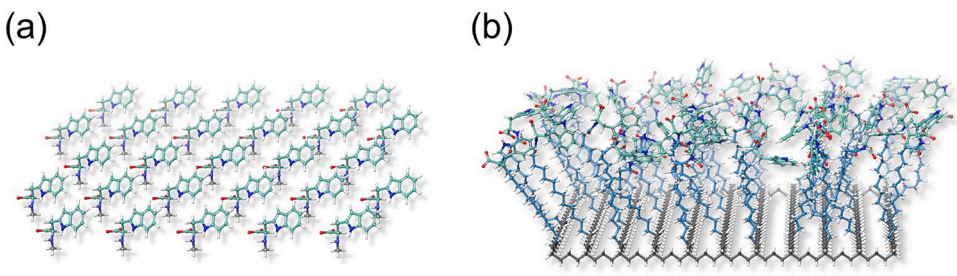

Fig. 2. Resin Models for Benchmarking - This figure displays two simplified models of the resin surface. SM1 (a) depicts ligands anchored in space, forming a planar surface, while SM2 (b) shows ligands attached to C12 carbon chains linked to a planar carbon surface.

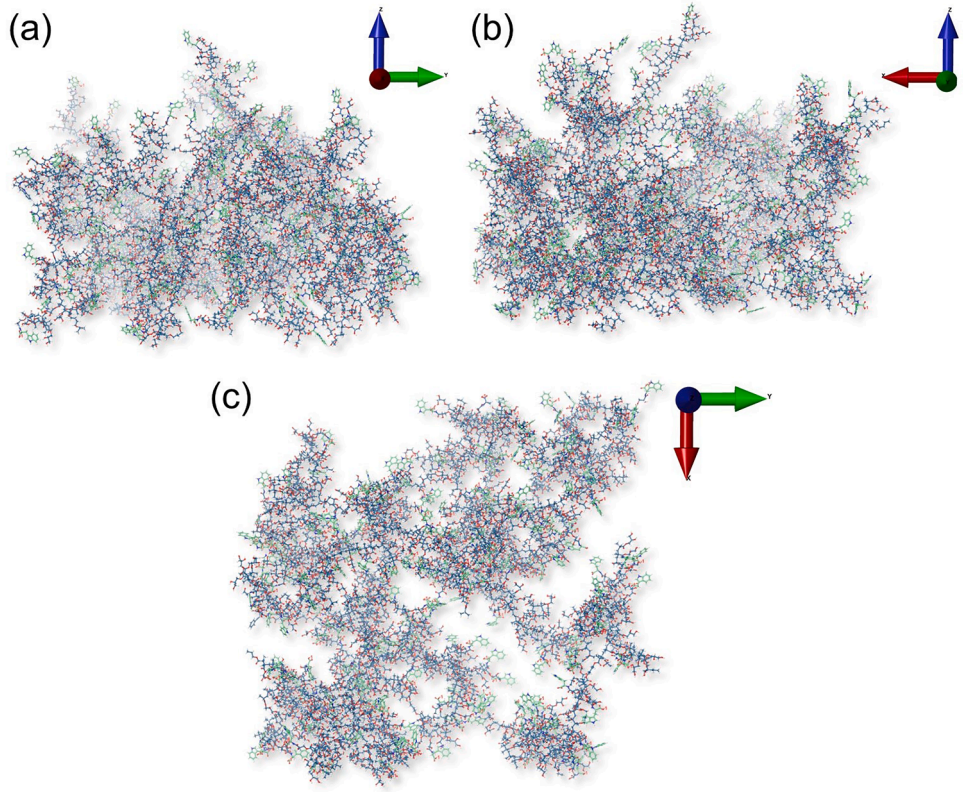

Fig. 3. All-Atom Model of MMC Resin Surface - This figure presents the AAM of the MMC Resin TOYOPEARL MX-Trp-650M. Carbon atoms from the methacrylic backbone are shown in blue and those from the Trp ligands in green. The panels (a) and (b) display side views of the resin surface along the z,y-plane and z,x-plane, respectively. Panel (c) offers a top view at the surface, showcasing mesopores penetrating the model.

AAM. Fig. 4a displays the pose following the docking simulation, where only one of the peptide's four positively charged amine groups engages in π-cation interactions and forms salt bridges with a tryptophan ligand. However, after the minimization step, as depicted in Fig. 4b, two additional tryptophan ligands are drawn towards the peptide's positive charge, resulting in a total of three tryptophan ligands forming π-cation interactions and salt bridges with the amine groups.

Furthermore, it was observed that the peptide's negatively charged carboxyl group, visible at the lower end in the figure, repels the ligands, causing them to move away from this group. Conversely, the polymer backbone moves closer to the carboxyl group post-minimization, forming hydrogen bonds and van der Waals interactions. This reorientation of the polymer backbone contributes to the stabilization of the binding pose. The mentioned conformational changes of the adsorbent are indicated with arrows in Fig. 4a. Green arrows show changes due to attracting forces while red arrows symbolize atomic movement caused by repelling forces.

At the end of the workflow, ΔG was determined for each of the four poses of every peptide. Notably, the variation in ΔG among these poses for individual peptides was significant. For some peptides, the difference between the highest and lowest calculated ΔG of the four poses was as minimal as 5 kcal/mol, while for others, it reached as high as 20 kcal/mol. This translated to percentile differences ranging from 10 % to 38 %, with an average variation of 27 % across the poses for each peptide. The average binding free energies of every peptide are depicted in Fig. 5b on the y-axis, with error bars representing the variation in these energies.

This observed variation in binding energies could be attributed to two main factors. On the one hand, the variation could stem from false positive or false negative binding poses. On the other hand, the variation in binding energies might also reflect the actual diversity in binding scenarios. Differences in binding domains, due to the non-uniform structure of the polymer backbone could contribute to these variations.

3.3. Model validation through Langmuir constant prediction

To validate our computational model, we applied the Langmuir isotherm equation to the collected adsorption isotherm data using OriginPro 2023. This model was chosen since the isotherms consistently displayed Langmuir-shaped adsorption behavior, with coefficients of determination for all fits being no lower than 0.94. From these fits, we derived the K_L for each peptide. The adsorption isotherms and their corresponding Langmuir fits are included in Fig. S2 (SI).

Fig. 5a presents the net charge of each peptide plotted against its corresponding K_L. This analysis reveals that in multi-modal chromatography, where both electrostatic and hydrophobic interactions are involved, there is no straightforward correlation between the net charge and K_L. Although peptides with a higher positive charge generally show higher K_L values, consistent with the negatively charged ligand, there are exceptions. Notably, a peptide with a net charge of zero exhibits the second-highest K_L. This deviation from a straightforward correlation underscores the complexity of interactions within multi-modal chromatography. While electrostatic interactions are typically more dominant, localized clusters of positive charges on peptides with overall low net charges can still demonstrate a strong affinity to the resin. Additionally, hydrophobic interactions, though secondary, can also contribute significantly to the overall binding affinity. Therefore, predicting binding behaviors solely based on the molecular structures of the target molecule can prove to be difficult. To circumvent an exclusive reliance on experimental methods for determining K_L, we focused on calculating ΔG. Following the theoretical framework established by Ghosal and Gupta, we explored the relationship between ΔG and K_L, which they posited should be logarithmic, particularly when K_L is expressed in molar units such as L/mol or L/mmol [52].

Fig. 5b showcases a plot comparing our calculated ΔG averaged over all four binding poses (ΔG_{av}) against the experimentally determined K_L

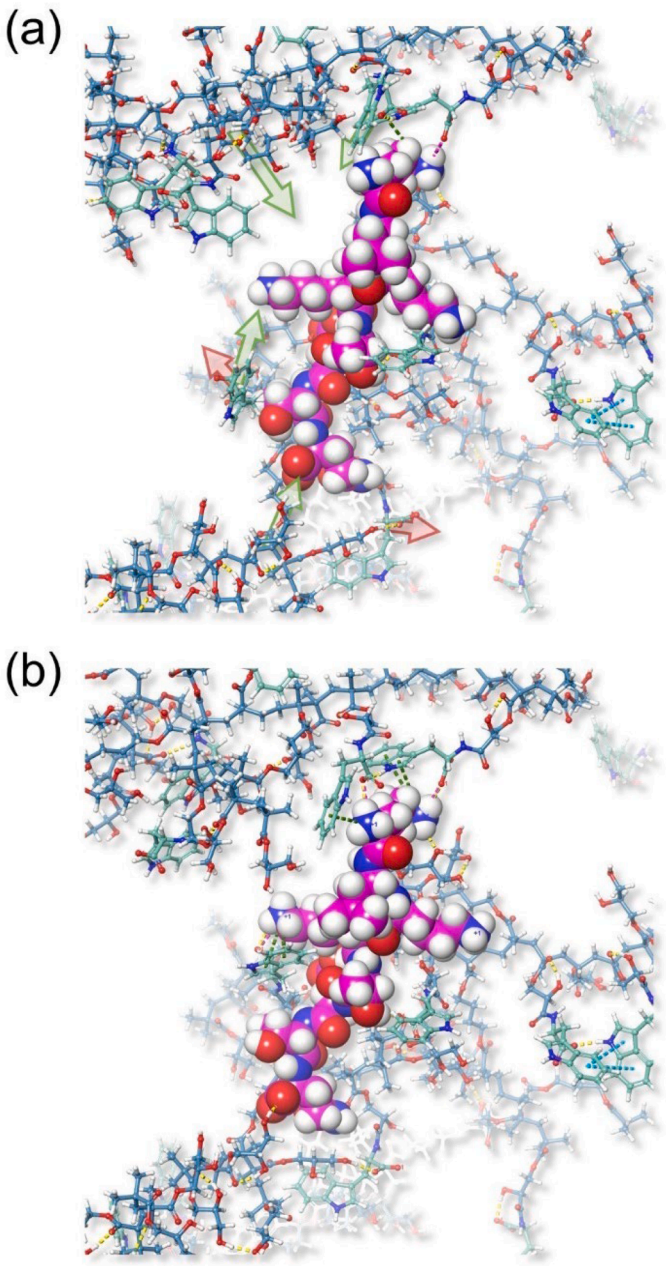

Fig. 4. Binding Pose of Octapeptide-2 with the AAM - Panel (a) displays the initial binding pose following the docking simulation, with future conformational changes indicated by arrows. Panel (b) shows the pose after minimization, emphasizing the reorientation of the polymer. The color-coded dotted lines represent different interaction types: pink for salt bridges, yellow for hydrogen bonds, green for π-cation, and blue for π-π interactions.

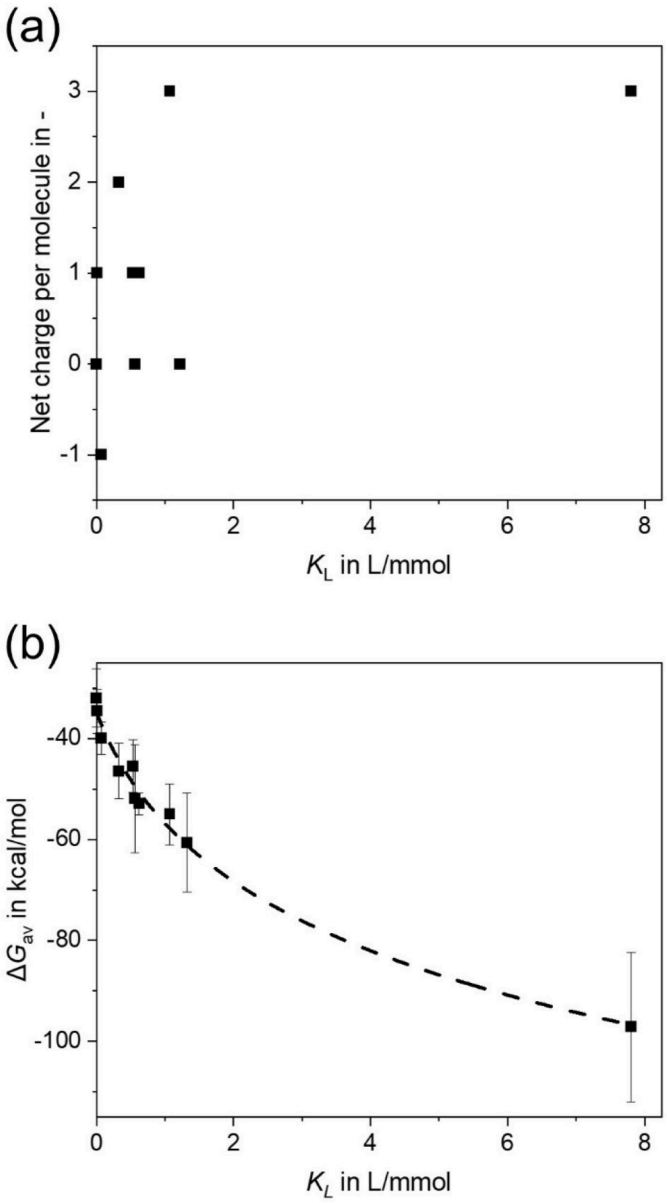

Fig. 5. Exploring the Correlation of K_L with Net Charges and Calculated Binding Free Energies - Panel (a) displays the relationship between each peptide's net charge at pH 4, determined using LigPrep (Schrödinger Release 2023-2), and its K_L, revealing no direct correlation. Panel (b) presents the relationship between K_L and ΔG_{av}, with a logarithmic relationship illustrated by the dotted line, established using three fitting parameters in OriginPro 2023.

for each peptide. The error bars on the y-axis indicate the variability in ΔG across the four distinct binding poses calculated for each peptide. The data demonstrates a strong logarithmic correlation between K_L and ΔG_{av}, with no apparent outliers. To analyze the relationship we used a three-parameter logarithmic model, details of which can be found in the SI. Notably, peptides with very low K_L values (less than 0.2 L/mmol) displayed corresponding ΔG_{av} values ranging from -40 to -32 kcal/mol. This range appears to represent a threshold for adsorption, suggesting that peptides require a minimum ΔG_{av} of about -40 kcal/mol to adsorb onto the resin effectively.

Further, to assess the predictive strength of our workflow, we performed a 2-fold cross-validation using MatlabR2023a, employing a logarithmic model with three fitting parameters. This method was selected for its effectiveness in providing a comprehensive assessment of the model's performance across two subsets of data. The results of this cross-validation are presented as black squares in Fig. 7. Here, the y-axis represents the K_L as predicted by our workflow, and the x-axis displays the experimentally measured true K_L. In a perfect model, all data points would align along the dotted line with a slope of 1. Our model achieved an R^2 of 0.96 and a root mean square error (RMSE) of 0.38 L/mmol, demonstrating strong predictive capabilities for Langmuir constants.

A notable strength of our model is its efficacy in predicting K_L values across a wide range, which is crucial for accurately forecasting both binding and elution conditions. By effectively predicting these conditions, our model offers a valuable tool for in silico screening of resins. This approach could streamline the resin selection process, allowing researchers to identify those resins with the most suitable binding and

elution characteristics for specific target molecules, thereby eliminating the need for extensive wet lab experimentation.

Additionally, we observed that for our peptides, the initial slope of the graph plotting the achieved loadings versus the corresponding equilibrium concentrations also exhibited a strong logarithmic correlation with the calculated ΔG_{av} values, achieving an R^2 of 0.88. This finding may prove valuable for analyzing systems for which the binding behavior strongly deviates from Langmuir adsorption behavior.

In conclusion, we aim to elucidate the limitations inherent in our modeling approach, specifically addressing why it does not extend to predicting the second parameter of the Langmuir isotherm, the maximum loading capacity (q_{max}). The distinction in our model's ability to predict K_L rather than q_{max} arises primarily from the nature of the parameters themselves and the data required to estimate them. The Langmuir constant reflects the affinity or strength of the interaction between the peptide and the resin [52]. This parameter can be directly derived from the binding free energy, which is computable from our molecular simulations. The relationship provides a clear thermodynamic pathway to estimate K_L based on the energetic landscape of the binding interactions. In contrast, q_{max} depends not only on the molecular interactions but also on the physical and morphological characteristics of the resin, such as surface area, pore size, and pore distribution, as well as the potential multilayer effects of target molecules. These factors affect how many molecules can physically and effectively bind to the resin at saturation. Since these are not parameters readily derived from our computational model, which is focused on energy calculations, they are not within the scope of the model's current capabilities.

Nonetheless, predicting K_L allows us to determine the affinity between peptides and chromatographic resins, which is essential for efficient separation processes. This capability enables the preliminary selection of the most appropriate resins, significantly reducing the need for extensive empirical testing. Moreover, since the affinity towards potential target molecules is essential for chromatography resins. Our approach could also be used for a rational design approach of chromatography resins, leading to custom-developed resins for difficult separation tasks. By providing a reliable computational approach to estimate K_L, our model serves as a valuable tool for guiding experimental setup, enhancing the predictability of peptide-resin interactions, and facilitating the development of more effective chromatographic systems. These benefits are particularly important in pharmaceutical and biochemical industries, where rapid and efficient process development can lead to substantial advancements and cost savings.

3.4. Comparison with state-of-the-art models

In this analysis, we aimed to compare the simulation results of our all-atom model with two simplified resin surface models, as shown in Fig. 2. We handed the docking grids of all three models as input to the workflow described in Chapter 2.3 to compute the binding energies with our target molecules. This demonstrated the versatility of our developed workflow by confirming its compatibility with various adsorbent models.

To elucidate the differences between the simplified models and our AAM, we analyzed the binding of Hexapeptide-9, which, despite having a net charge of zero, exhibits the second-highest measured K_L. Fig. 6a and b showcase the binding pose of Hexapeptide-9 with SM2 and the AAM, respectively. In these figures, the peptide residues are color-coded to indicate their contribution to the overall binding energy, with the spectrum ranging from red to green. Redder hues signify repulsion from the adsorbent model, while greener hues indicate stronger attraction. Fig. 6c presents an analysis of the binding energies, breaking down the contributions of Coulomb and van der Waals (vdW) interactions, along

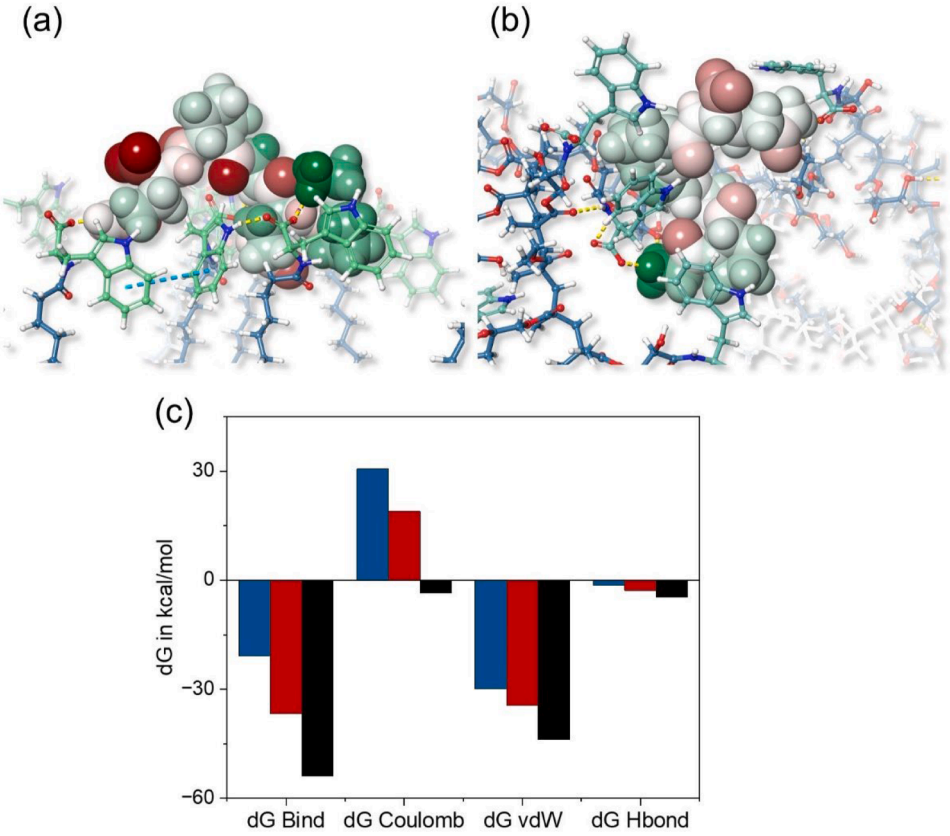

Fig. 6. Binding Energy Analysis of Hexapeptide-9 - Panel (a) and Panel (b) display the binding poses of Hexapeptide-9 with SM2 and the AAM, respectively, with peptide residues color-coded based on their contribution to ΔG. Panel (c) compares the ΔG of Hexapeptide-9 with the SM1 (blue), SM2 (red), and AAM (black), detailing the contributions of Coulomb, and vdW interactions, as well as hydrogen bonds, averaged over all calculated poses.

with hydrogen bonds, averaged across all four poses calculated for Hexapeptide-9. A notable observation is the heightened Coulomb interactions in the simplified models compared to the AAM. In SM1 and SM2, the presence of Hexapeptide-9′s negatively charged carboxyl group leads to overall positive Coulomb interactions due to repulsion. In contrast, the AAM demonstrates slightly negative overall Coulomb interactions due to attraction with the positively charged amine group. This difference could stem from the distinct ligand orientations and flexibilities in each model. Despite similar ligand densities, the way ligands are exposed and oriented in SM1 and SM2 facilitates more effective electrostatic interactions with charged groups. This contrasts with the AAM, where the ligands' orientation and flexibility are modulated by the surrounding polymer backbone. The flexibility of the backbone also allows the ligands to move away from negative patches, towards positive charges as shown in Fig. 4. This trend was not isolated to a single peptide but was observed across various peptides, indicating a systematic difference in how the electrostatic interactions are influenced by the presence of the polymer backbone.

Furthermore, the polymeric backbone in the all-atom model played a significant role in binding energy, contributing notably through vdW interactions. Therefore, the AAM registered the highest overall binding energy, while SM1 and SM2 exhibited considerably lower values. Consequently, for peptides with a more positive charge, the opposite trend was observed, with SM1 and SM2 often showing higher binding energies than the AAM, since the exposed ligands allow stronger electrostatic attraction.

3.5. Benchmarking the workflows

In this final analysis, we begin by benchmarking the predictive capability for Langmuir constants of our AAM against the two simplified resin surface models, as part of evaluating the workflows developed in this study. This assessment involved performing a cross-validation for each model, as described in Chapter 3.3 for the AAM.

Fig. 7a displays the validation plot for all three models. A key observation was that both simplified models, SM1 and SM2, each have significant outliers. Specifically, for SM1, Acetyl Tetrapeptide-3 is an outlier, and for SM2, it is Octapeptide-1, with net charges of 1 and 3, respectively. In both cases, the predicted K_L values are markedly higher than the experimentally determined K_L. For a more detailed examination of the lower K_L values, Fig. 7b offers a zoomed-in view of Fig. 7a. This closer look reveals that the data points from SM 1 and SM 2 consistently deviate further from the dotted line, which represents ideal predictions, in comparison to those from the AAM. Interestingly, SM1 and SM2 tend to overpredict K_L for peptides with more positive charges and underpredict for those with neutral or negative charges. This trend correlates with the findings from the previous chapter, where the simplified models showed elevated ΔG for positively charged and lower ΔG for more negatively charged peptides compared to the AAM. Additionally, it was noted that SM1 and SM2 demonstrate greater prediction accuracy for lower K_L values compared to higher K_L values. This characteristic renders them more suitable for predicting elution conditions rather than binding conditions in chromatographic applications.

To quantitatively assess the predictive capabilities of the models, Fig. 8 includes three bars on the right side, each representing the RMSE for the all-atom model and the two simplified models. Here, SM1 demonstrates the lowest precision in predictions with an RMSE of 5.49 L/mmol, while SM2 exhibits a notable improvement in predictive accuracy. This increase in accuracy is likely due to the enhanced ligand flexibility in SM2, leading to a more heterogeneous surface configuration, a feature that distinctly sets it apart from SM1. The AAM surpasses both simplified models, achieving the lowest RMSE. This enhanced accuracy could be attributed to the more realistic representation of the resin surface, achieved by incorporating the polymer backbone into the model.

In our second benchmarking analysis, we compared our workflow for

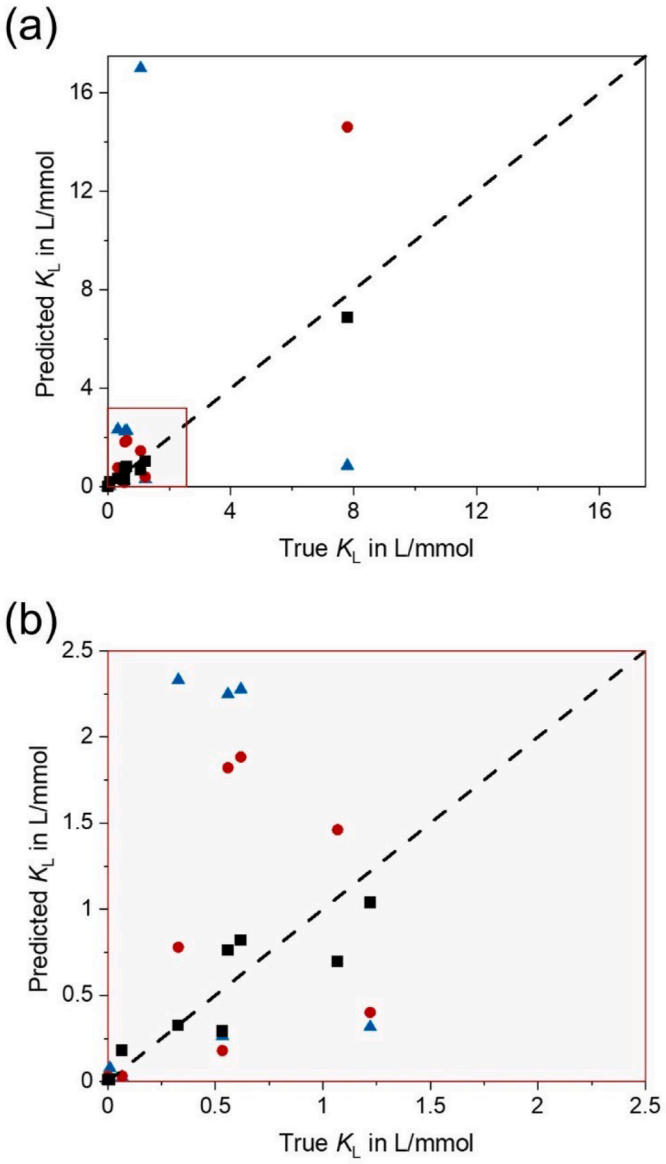

Fig. 7. Validation Plots for Model Comparisons - Panel (a) displays the cross-validation results for the AAM (black squares) and the two simplified models of the resin surface, SM 1 (red circles) and SM 2 (blue triangles), showing predicted K_L values against experimentally determined K_L. Panel (b) offers a zoomed-in view of the same plot.

calculating ΔG_{av} with an established method that solely integrates Glide docking and consecutive MM-GBSA calculations for determining peptide binding energies [36]. Fig. 8 presents this comparison, where the left side bars indicate the RMSE for K_L predictions using the established workflow. A notable observation from this comparison is that all models exhibit higher RMSE values when analyzed with this conventional method compared to our newly developed workflow. SM 1 showed the highest RMSE in both workflows, indicating its highly structured design might fail to mimic the real resin surface's complexity accurately. Furthermore, both SM2 and AAM models exhibited RMSEs above 4 L/mmol with the conventional method, which is significantly higher than the average K_L of 1.3 L/mmol observed across the peptides, indicating an inadequacy in providing accurate predictions. This underscores how the effectiveness of a model can significantly vary depending on the computational method used.

A key advantage of our workflow is its ability to account for the flexibility of the resin's polymer backbone. This was achieved through a

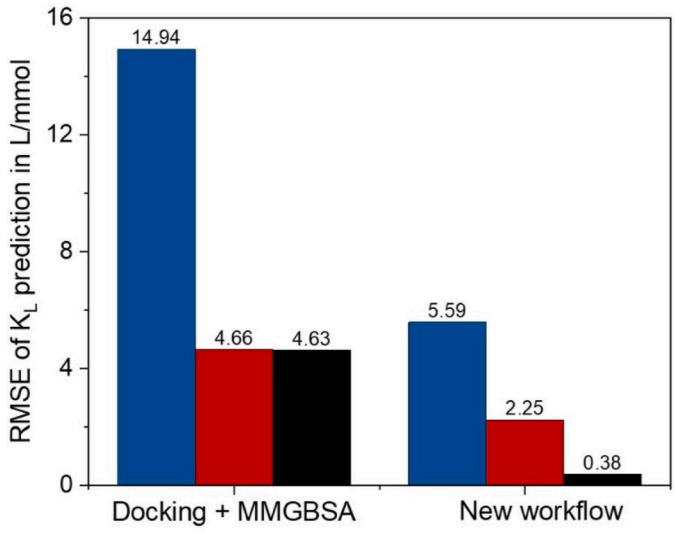

Fig. 8. RMSE Comparison of Modeling Approaches - This figure displays the RMSE for K_L predictions across different models. The left side bars represent RMSE for the established Glide docking and MM-GBSA workflow, while the right side bars show RMSE for our presented workflow. The RMSE of the AAM is displayed in black bars and of the SM1 and SM2 in blue and red bars, respectively.

minimization step, which allows the resin surface to adapt upon peptide adoption. With this approach, the computational demand was maintained comparatively low, especially when contrasted with time-resolved molecular dynamics simulations. Additionally, our workflow incorporates electronic structure effects by utilizing a semiempirical QM method. These enhancements are likely key contributors to the superior performance of the AAM, as it surpasses SM2 in accuracy only when these aspects are considered. These benchmarking exercises demonstrate the importance of selecting appropriate computational methods that align with the specific characteristics and complexities of the models being used, especially in applications involving intricate molecular interactions such as in chromatography.

4. Conclusion and further directions

In this study we successfully introduced and validated two innovative workflows designed for predicting peptide binding behaviors in multimodal chromatography, focusing on methacrylate-based resins. Utilizing the first workflow, we were able to generate a detailed all-atom model of an MMC resin surface, incorporating the polymethacrylic backbone. With 15 nm in diameter, the model can be utilized to calculate interactions with a wide range of biomolecules.

To showcase the innovative capabilities of our model, we developed and deployed a unique workflow tailored specifically for rapid binding free energy calculations with linear peptides. This novel workflow leverages computationally efficient techniques that facilitate swift and precise predictions of experimental K_L values, making it highly suitable for use on standard office computers. Employing this advanced workflow, our custom-developed all-atom model markedly surpasses the performance of traditional, simplified models, consistently delivering enhanced predictive accuracy. This progression represents a significant advancement in the application of computational modeling to understand and predict chromatographic behaviors, offering a powerful tool for the rapid evaluation and optimization of chromatographic systems.

Looking ahead, our research will delve into exploring how the composition of resin building blocks influences simulation outcomes. This will include a focus on variables such as ligand density, the degree of crosslinking, and the integration of spacer molecules. Additionally, it is important to note that the Glide docking step is currently limited to handling molecules with no more than 500 atoms or 100 rotatable bonds. Consequently, this restriction confines the current scope of the workflow primarily to smaller biomolecules, such as linear peptides, while larger biomolecules like proteins fall outside its capabilities. Therefore, our future work will aim to expand the workflow to accommodate proteins of varying sizes, thereby enhancing its applicability and relevance in the broader field of chromatographic research.

CRediT authorship contribution statement

Tim Ballweg: Writing – original draft, Visualization, Validation, Software, Methodology, Investigation, Conceptualization. **Modan Liu:** Writing – review & editing, Visualization, Software, Methodology, Investigation. **Julian Grimm:** Methodology, Investigation. **Elaheh Sedghamiz:** Software, Methodology, Investigation. **Wolfgang Wenzel:** Writing – review & editing, Conceptualization. **Matthias Franzreb:** Writing – review & editing, Conceptualization.

Declaration of competing interest

The authors declare that they have no known competing financial interests or personal relationships that could have appeared to influence the work reported in this paper.

Data availability

Data will be made available on request.

Acknowledgments

The authors express their gratitude to the "Virtual Materials Design" (VirtMat) initiative at the Karlsruhe Institute of Technology (KIT), funded by the Helmholtz Association, within the Joint Lab VMD, for funding this work. Additionally, this work was co-funded by the KIT Strategic Project Auto.MAP.

Supplementary materials

Supplementary material associated with this article can be found, in the online version, at doi:10.1016/j.chroma.2024.465089.

References

[1] G. Guiochon, L.A. Beaver, Separation science is the key to successful biopharmaceuticals, J. Chromatogr. A 1218 (2011) 8836–8858, https://doi.org/10.1016/j.chroma.2011.09.008.
[2] G.L. Losacco, M.B. Hicks, J.O. DaSilva, H. Wang, M. Potapenko, F.R. Tsay, I.A. H. Ahmad, I. Mangion, D. Guillarme, E.L. Regalado, Automated ion exchange chromatography screening combined with in silico multifactorial simulation for efficient method development and purification of biopharmaceutical targets, Anal. Bioanal. Chem. 414 (2022) 3581–3591, https://doi.org/10.1007/s00216-022-03982-z.
[3] D.K. Babi, J. Griesbach, S. Hunt, F. Insaidoo, D. Roush, R. Todd, A. Staby, J. Welsh, F. Wittkopp, Opportunities and challenges for model utilization in the biopharmaceutical industry: current versus future state, Curr. Opin. Chem. Eng. 36 (2022) 100813, https://doi.org/10.1016/j.coche.2022.100813.
[4] H. Schmidt-Traub, M. Schulte, A. Seidel-Morgenstern, H. Schmidt-Traub, Preparative Chromatography, Wiley Online Library, 2012.
[5] G. Zhao, X.Y. Dong, Y. Sun, Ligands for mixed-mode protein chromatography: principles, characteristics and design, J. Biotechnol. 144 (2009) 3–11, https://doi.org/10.1016/j.jbiotec.2009.04.009.
[6] K. Zhang, X. Liu, Mixed-mode chromatography in pharmaceutical and biopharmaceutical applications, J. Pharm. Biomed. Anal. 128 (2016) 73–88, https://doi.org/10.1016/j.jpba.2016.05.007.
[7] W.S. Hancock, J.T. Sparrow, Use of mixed-mode, high-performance liquid chromatography for the separation of peptide and protein mixtures, J. Chromatogr. 206 (1981) 71–82, https://doi.org/10.1016/S0021-9673(00)82606-0.
[8] R. Muca, D. Antos, Protein association on multimodal chromatography media, J. Chromatogr. A 1691 (2023) 463827, https://doi.org/10.1016/j.chroma.2023.463827.

[9] K. Kallberg, H.O. Johansson, L. Bulow, Multimodal chromatography: an efficient tool in downstream processing of proteins, Biotechnol. J. 7 (2012) 1485–1495, https://doi.org/10.1002/biot.201200074.

[10] F. Dismer, J. Hubbuch, 3D structure-based protein retention prediction for ion-exchange chromatography, J. Chromatogr. A 1217 (2010) 1343–1353, https://doi.org/10.1016/j.chroma.2009.12.061.

[11] A.A. Shukla, S. Rameez, L.S. Wolfe, N. Oien, High-throughput process development for biopharmaceuticals, Adv. Biochem. Eng. Biotechnol 165 (2018) 401–441, https://doi.org/10.1007/10_2017_20.

[12] J.C. Giddings, The role of lateral diffusion as a rate-controlling mechanism in chromatography, J. Chromatogr. A 5 (1961) 46–60, https://doi.org/10.1016/S0021-9673(01)92815-8.

[13] J.J. van Deemter, F.J. Zuiderweg, A. Klinkenberg, Longitudinal diffusion and resistance to mass transfer as causes of nonideality in chromatography, Chem. Eng. Sci. 5 (1956) 271–289, https://doi.org/10.1016/0009-2509(56)80003-1.

[14] E. Glueckauf, Theory of chromatography. Part 10.—Formulæ for diffusion into spheres and their application to chromatography, Trans. Faraday Soc. 51 (1955) 1540–1551, https://doi.org/10.1039/TF9555101540.

[15] P. Schneider, J.M. Smith, Adsorption rate constants from chromatography, AIChE J. 14 (1968) 762–771, https://doi.org/10.1002/aic.690140516.

[16] C. Horvath, H.J. Lin, Band spreading in liquid chromatography, J. Chromatogr. A 149 (1978) 43–70, https://doi.org/10.1016/S0021-9673(00)80978-4.

[17] C.A. Brooks, S.M. Cramer, Steric mass-action ion exchange: displacement profiles and induced salt gradients, AIChE J. 38 (1992) 1969–1978, https://doi.org/10.1002/aic.690381212.

[18] H.S. Karkov, L. Sejergaard, S.M. Cramer, Methods development in multimodal chromatography with mobile phase modifiers using the steric mass action model, J. Chromatogr. A 1318 (2013) 149–155, https://doi.org/10.1016/j.chroma.2013.10.004.

[19] R. Hess, D. Yun, D. Saleh, T. Briskot, J.H. Grosch, G. Wang, T. Schwab, J. Hubbuch, Standardized method for mechanistic modeling of multimodal anion exchange chromatography in flow through operation, J. Chromatogr. A 1690 (2023) 463789, https://doi.org/10.1016/j.chroma.2023.463789.

[20] D.T. Stanton, P.C. Jurs, Development and use of charged partial surface area structural descriptors in computer-assisted quantitative structure-property relationship studies, Anal. Chem. 62 (1990) 2323–2329.

[21] G. Sagandykova, B. Buszewski, Perspectives and recent advances in quantitative structure-retention relationships for high performance liquid chromatography. How far are we? TrAC Trends Anal. Chem. 141 (2021) 116294 https://doi.org/10.1016/j.trac.2021.116294.

[22] Y.R. Singh, D.B. Shah, D.G. Maheshwari, J.S. Shah, S. Shah, Advances in AI-driven retention prediction for different chromatographic techniques: unraveling the complexity, Crit. Rev. Anal. Chem. (2023) 1–11, https://doi.org/10.1080/10408347.2023.2254379.

[23] R. Hess, J. Faessler, D. Yun, D. Saleh, J.H. Grosch, T. Schwab, J. Hubbuch, Antibody sequence-based prediction of pH gradient elution in multimodal chromatography, J. Chromatogr. A 1711 (2023) 464437, https://doi.org/10.1016/j.chroma.2023.464437.

[24] F. Dismer, M. Petzold, J. Hubbuch, Effects of ionic strength and mobile phase pH on the binding orientation of lysozyme on different ion-exchange adsorbents, J. Chromatogr. A 1194 (2008) 11–21, https://doi.org/10.1016/j.chroma.2007.12.085.

[25] R. Sardella, E. Camaioni, A. Macchiarulo, A. Gioiello, M. Marinozzi, A. Carotti, Computational studies in enantioselective liquid chromatography: forty years of evolution in docking- and molecular dynamics-based simulations, TrAC Trends Anal. Chem. 122 (2020) 115703, https://doi.org/10.1016/j.trac.2019.115703.

[26] S. Parimal, S. Garde, S.M. Cramer, Interactions of multimodal ligands with proteins: insights into selectivity using molecular dynamics simulations, Langmuir 31 (2015) 7512–7523, https://doi.org/10.1021/acs.langmuir.5b00236.

[27] F. Dismer, J. Hubbuch, A novel approach to characterize the binding orientation of lysozyme on ion-exchange resins, J. Chromatogr. A 1149 (2007) 312–320, https://doi.org/10.1016/j.chroma.2007.03.074.

[28] S. Banerjee, S. Parimal, S.M. Cramer, A molecular modeling based method to predict elution behavior and binding patches of proteins in multimodal chromatography, J. Chromatogr. A 1511 (2017) 45–58, https://doi.org/10.1016/j.chroma.2017.06.059.

[29] M.J. Benes, D. Horák, F. Svec, Methacrylate-based chromatographic media, J. Sep. Sci. 28 (2005) 1855–1875, https://doi.org/10.1002/jssc.200500186.

[30] T. Arakawa, Isoform separation by a mixed-mode resin, TOYOPEARL MX-Trp-650M, Curr. Protein Pept. Sci. 20 (2019) 61–64, https://doi.org/10.2174/1389203718666171009111355.

[31] E. Sedghamiz, M. Liu, W. Wenzel, Challenges and limits of mechanical stability in 3D direct laser writing, Nat. Commun. 13 (2022) 2115, https://doi.org/10.1038/s41467-022-29749-9.

[32] L.S. Dodda, I. Cabeza de Vaca, J. Tirado-Rives, W.L. Jorgensen, LigParGen web server: an automatic OPLS-AA parameter generator for organic ligands, Nucleic Acids Res. 45 (2017) W331–W336, https://doi.org/10.1093/nar/gkx312.

[33] W.L. Jorgensen, D.S. Maxwell, J. Tirado-Rives, Development and testing of the OPLS all-atom force field on conformational energetics and properties of organic liquids, J. Am. Chem. Soc. 118 (1996) 11225–11236, https://doi.org/10.1021/ja9621760.

[34] C.R.C. Rêgo, J. Schaarschmidt, T. Schlöder, M. Penaloza-Amion, S. Bag, T. Neumann, T. Strunk, W. Wenzel, SimStack: an intuitive workflow framework, Front. Mater. 9 (2022) 877597, https://doi.org/10.3389/fmats.2022.877597.

[35] A.P. Thompson, H.M. Aktulga, R. Berger, D.S. Bolintineanu, W.M. Brown, P. S. Crozier, P.J. Int Veld, A. Kohlmeyer, S.G. Moore, T.D. Nguyen, R. Shan, M. J. Stevens, J. Tranchida, C. Trott, S.J. Plimpton, LAMMPS - a flexible simulation tool for particle-based materials modeling at the atomic, meso, and continuum scales, Comput. Phys. Commun. 271 (2022) 108171, https://doi.org/10.1016/j.cpc.2021.108171.

[36] I. Tubert-Brohman, W. Sherman, M. Repasky, T. Beuming, Improved docking of polypeptides with Glide, J. Chem. Inf. Model. 53 (2013) 1689–1699, https://doi.org/10.1021/ci400128m.

[37] C. Lu, C. Wu, D. Ghoreishi, W. Chen, L. Wang, W. Damm, G.A. Ross, M.K. Dahlgren, E. Russell, C.D. von Bargen, R. Abel, R.A. Friesner, E.D. Harder, OPLS4: improving force field accuracy on challenging regimes of chemical space, J. Chem. Theory Comput. 17 (2021) 4291–4300, https://doi.org/10.1021/acs.jctc.1c00302.

[38] C. Bannwarth, S. Ehlert, S. Grimme, GFN2-xTB-an accurate and broadly parametrized self-consistent tight-binding quantum chemical method with multipole electrostatics and density-dependent dispersion contributions, J. Chem. Theory Comput. 15 (2019) 1652–1671, https://doi.org/10.1021/acs.jctc.8b01176.

[39] J. Gorges, B. Bädorf, S. Grimme, A. Hansen, Efficient computation of the interaction energies of very large non-covalently bound complexes, Synlett 34 (2023) 1135–1146, https://doi.org/10.1055/s-0042-1753141.

[40] C. Bannwarth, E. Caldeweyher, S. Ehlert, A. Hansen, P. Pracht, J. Seibert, S. Spicher, S. Grimme, Extended tight-binding quantum chemistry methods, WIREs Comput. Mol. Sci. 11 (2021) e1493, https://doi.org/10.1002/wcms.1493.

[41] Y.Q. Chen, Y.J. Sheng, Y.Q. Ma, H.M. Ding, Efficient calculation of protein-ligand binding free energy using GFN methods: the power of the cluster model, Phys. Chem. Chem. Phys. 24 (2022) 14339–14347, https://doi.org/10.1039/D2CP00161F.

[42] S. Decherchi, A. Cavalli, Thermodynamics and kinetics of drug-target binding by molecular simulation, Chem. Rev. 120 (2020) 12788–12833, https://doi.org/10.1021/acs.chemrev.0c00.

[43] J.H. Jensen, Predicting accurate absolute binding energies in aqueous solution: thermodynamic considerations for electronic structure methods, Phys. Chem. Chem. Phys. 17 (2015) 12441–12451, https://doi.org/10.1039/C5CP00628G.

[44] T. Herrmann, M. Schröder, J. Hubbuch, Generation of equally sized particle plaques using solid-liquid suspensions, Biotechnol. Prog. 22 (2006) 914–918, https://doi.org/10.1021/bp050296i.

[45] J. Kittelmann, K.M.H. Lang, M. Ottens, J. Hubbuch, An orientation sensitive approach in biomolecule interaction quantitative structure-activity relationship modeling and its application in ion-exchange chromatography, J. Chromatogr. A 1482 (2017) 48–56, https://doi.org/10.1016/j.chroma.2016.12.065.

[46] K.M.H. Lang, J. Kittelmann, C. Dürr, A. Osberghaus, J. Hubbuch, A comprehensive molecular dynamics approach to protein retention modeling in ion exchange chromatography, J. Chromatogr. A 1381 (2015) 184–193, https://doi.org/10.1016/j.chroma.2015.01.018.

[47] K.M.H. Lang, J. Kittelmann, F. Pilgram, A. Osberghaus, J. Hubbuch, Custom-tailored adsorbers: a molecular dynamics study on optimal design of ion exchange chromatography material, J. Chromatogr. A 1413 (2015) 60–67, https://doi.org/10.1016/j.chroma.2015.08.021.

[48] J. Zhou, H.K. Tsao, Y.J. Sheng, S. Jiang, Monte Carlo simulations of antibody adsorption and orientation on charged surfaces, J. Chem. Phys. 121 (2004) 1050–1057, https://doi.org/10.1063/1.1757434.

[49] J. Liang, G. Fieg, F.J. Keil, S. Jakobtorweihen, Adsorption of proteins onto ion-exchange chromatographic media: a molecular dynamics study, Ind. Eng. Chem. Res. 51 (2012) 16049–16058, https://doi.org/10.1021/ie301407b.

[50] L. Zhang, G. Zhao, Y. Sun, Molecular insight into protein conformational transition in hydrophobic charge induction chromatography: a molecular dynamics simulation, J. Phys. Chem. B 113 (2009) 6873–6880, https://doi.org/10.1021/jp809754k.

[51] L. Zhang, G. Zhao, Y. Sun, Effects of ligand density on hydrophobic charge induction chromatography: molecular dynamics simulation, J. Phys. Chem. B 114 (2010) 2203–2211, https://doi.org/10.1021/jp903852c.

[52] P.S. Ghosal, A.K. Gupta, Determination of thermodynamic parameters from Langmuir isotherm constant-revisited, J. Mol. Liq. 225 (2017) 137–146, https://doi.org/10.1016/j.molliq.2016.11.058.